SOTHNODYML-2024 IOP Publishing
Journal of Physics: Conference Series **3002** (2025) 012002 doi:10.1088/1742-6596/3002/1/012002

Images of a thin accretion disk around Kerr Black Hole with synchronized scalar hair

Galin N. Gyulchev[1], **Lucas G. Collodel**[2], **Stoytcho S. Yazadjiev**[1], **Daniela D. Doneva**[2], **Petya G. Nedkova**[1]

[1]Department of Theoretical Physics, Faculty of Physics, Sofia University, Sofia 1164, Bulgaria

[2]Theoretical Astrophysics, Eberhard Karls University of Tübingen, Tübingen 72076, Germany

E-mail: gyulchev@phys.uni-sofia.bg

Abstract. We study possible observable images of a thin accretion disk around rotating hairy black holes with two non-trivial time-periodic scalar fields. Such black holes are a viable alternative to the Kerr black hole, having a much more complicated geodesic structure and resulting accretion disks. We investigate how the different amounts of scalar hair around the black holes, quantified by a normalized charge, alter the direct and indirect images of the disk. Our results show that for high values of this charge, close to a boson star limit, chaotic disk images are observed with multiple small, disconnected components. For moderately large amounts of scalar hair and corresponding normalized charge, although the images still exhibit chaotic behavior, a dominant central dark region component emerges. For lower values of the normalized charge, the accretion disk images qualitatively resemble those for the Kerr black hole.

1 Introduction

In 2019, the EHT revealed the first image of the supermassive black hole at the center of M87 [1], followed by the imaging of Sgr A* in 2022 [2]. These observations have inspired theoretical studies challenging the validity of the Kerr black hole model and investigating alternative scenarios, including horizonless objects [3, 4, 5, 6, 7] and solutions proposed by modified gravity theories [8, 9, 10, 11, 12, 13, 14].

Alternative models for black holes, such as Kerr counterparts, often exhibit unique and distinguishable traits in their accretion disk images and shadow structures. These include features like highly distorted shadows or configurations with multiple disconnected regions [15, 16, 17]. Some notable examples involve black holes that possess scalar or Proca fields [18, 19, 22], are part of binary systems [23, 24, 25], or are influenced by surrounding matter [26, 27, 28]. The present work focuses on scalarized black holes that interact with two scalar fields synchronized to the rotation of the black hole.

It is also well-known that black holes can not support scalar hair of a single stationary and minimally coupled scalar field. However, when multiple scalar fields are introduced, it becomes possible for black holes with synchronized scalar configurations to form [29] when the scalar fields are periodic in time and in the azimuthal coordinate. Such configurations can even arise in target spaces with curved geometry [30, 31, 32, 33]. This study examines solutions specifically in target spaces with zero Gaussian curvature [18, 19] and explores how the normalized charge influences the appearance of accretion disks and the associated shadows, particularly when viewed from non-equatorial inclinations.

The paper is organized as follows: Section 2 discusses scalarized black holes, Section 3 outlines the theory of accretion disk imaging, and Section 4 examines the influence of the normalized charge on images of thin accretion disks around black holes, followed by our conclusions.

2 Kerr black holes with synchronized scalar hair

We conisder a gravitational theory with metric tensor $g_{\mu\nu}$ and two dynamic scalar fields, $\varphi^a = (\varphi^1, \varphi^2)$, minimally coupled to Einstein's gravity. These scalar fields can be interpreted as generalized coordinates on a two-dimensional Riemannian manifold $(\mathcal{E}_2, \gamma_{ab}(\varphi))$, known as the target space, characterized by a positive-definite metric $\gamma_{ab}(\varphi)$. The action for this theory is given by

$$S = \frac{1}{4\pi G} \int \sqrt{-g} \left(\frac{R}{4} - \frac{1}{2} g^{\mu\nu} \gamma_{ab}(\varphi) \partial_\mu \varphi^a \partial_\nu \varphi^b - V(\varphi) \right) d^4x, \tag{1}$$

where $V(\varphi)$ denotes the potential associated with the scalar fields. This action describes the vacuum action of tensor-multi-scalar theories of gravity [20, 21]. By varying this action with respect to the spacetime metric and the scalar fields, we obtain the following field equations:

$$\begin{aligned} R_{\mu\nu} &= 2\gamma_{ab}(\varphi)\partial_\mu \varphi^a \partial_\nu \varphi^b + 2V(\varphi) g_{\mu\nu}, & (2) \\ \Box \varphi^a &= -\gamma^a_{bc}(\varphi) g^{\mu\nu} \partial_\mu \varphi^b \partial_\nu \varphi^c + \gamma^{ab}(\varphi) \frac{\partial V(\varphi)}{\partial \varphi^b}. & (3) \end{aligned}$$

In this context, $\Box \equiv g^{\mu\nu}\nabla_\mu \nabla_\nu$ represents the d'Alembert operator linked to the spacetime metric, and $\gamma^a_{bc}(\varphi)$ are the Christoffel symbols for the metric of the target space.

We consider two scalar fields, with maximally symmetric target spaces $(\mathcal{E}_2, \gamma_{ab}(\varphi))$. In isothermal coordinates, the target space metric is conformally flat:

$$\gamma_{ab}(\varphi) = \Omega^2(\varphi)\delta_{ab}, \tag{4}$$

where δ_{ab} is the Kronecker delta, and the conformal factor is

$$\Omega^2(\varphi) = \frac{1}{\left(1 + \frac{\kappa}{4}\psi^2\right)^2}, \tag{5}$$

with $\psi^2 = \delta_{ab}\varphi^a \varphi^b$ and κ being the Gaussian curvature of the target space.

For the scalar field potential, we assume a standard massive form

$$V(\psi) = \frac{1}{2}\mu^2 \psi^2, \tag{6}$$

where μ is the scalar field mass. In the special case of zero Gaussian curvature ($\kappa = 0$) the model corresponds to that described in [18].

In order to study rotating black holes, we employ the following ansatz for a stationary and axisymmetric spacetime line element:

$$ds^2 = -\mathcal{N} e^{2F_0} dt^2 + e^{2F_1} \left(\frac{dr^2}{\mathcal{N}} + r^2 d\theta^2 \right) + e^{2F_2} r^2 \sin^2\theta \left(d\phi - \frac{\omega}{r} dt \right)^2, \tag{7}$$

where $\mathcal{N} = 1 - \frac{r_H}{r}$, with r_H denoting the location of the event horizon in these coordinates. The functions F_0, F_1, F_2, and ω depend only on the variables r and θ.

This paper investigates black holes with scalar fields. To circumvent the no-scalar-hair theorems, it is essential that the scalar fields are time-dependent, with multiple scalar fields involved [34]. We propose the following ansatz:

$$\varphi^1 = \psi(r,\theta)\cos(\omega_s t + m\phi), \quad \varphi^2 = \psi(r,\theta)\sin(\omega_s t + m\phi), \tag{8}$$

which is consistent with the circular symmetry of the metric in equation (7) and ensures that the field equations in (2) and (3) remain stationary. Here, ω_s is a real parameter and m is an integer. Further details can be found in [29].

Using specific forms for the scalar field and metric ansatz, along with boundary conditions of regularity at the event horizon, along the axes, and asymptotic flatness, leads to stationary black hole solutions with nontrivial scalar hair. The regularity condition prevents scalar flux into the black hole, requiring synchronization between the scalar field oscillations and the black hole's rotation [35].

We introduce the normalized charge $q = \frac{mQ}{J}$ as a measure of hairiness, where Q, denotes the conserved Noether charge, a key quantity used to characterize Kerr black holes with synchronized scalar hair [18].

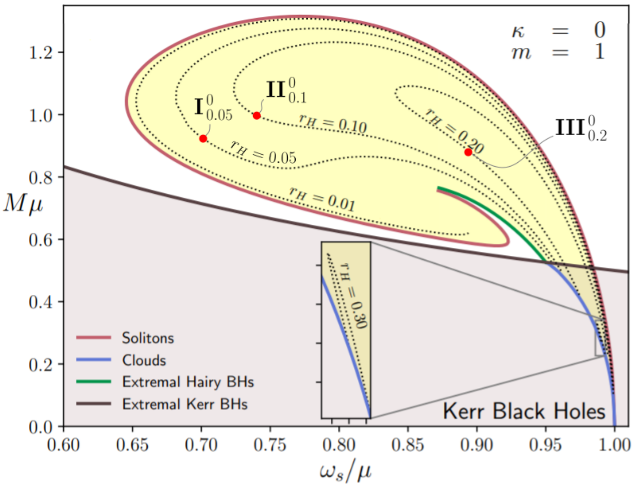

Figure 1: In the $M - \omega_s$ plane, we present solution curves for fixed r_H from [29] with $\kappa = 0$. The black curve represents Kerr solutions, while the yellow region highlights exotic configurations affected by r_H and the normalized charge $q = \frac{mQ}{J}$. Red points indicate solutions with varying values of q. Configurations are labeled as $\mathbf{X}^{0}_{v}$, where 0 corresponds to κ and v represents the value of r_H. Further details of these solutions can be found in Table 1 of the Appendix.

The angular momentum of the scalar field is quantized as $J_\psi = mQ$, which leads to the expression $q = \frac{J_\psi}{J}$. Solutions with $q \approx 0$ represent scalar clouds that do not backreact on the metric, while the boson star limit corresponds to $q \approx 1$, [36, 37].

Using numerical solutions from [29] for $\kappa = 0$ and a fixed $m = 1$, this paper considers the regions of existence of hairy black holes in $M - \omega_s$ plane (Fig. 1). The extremal Kerr limit, shown by the black line where $a = M$, indicates that Kerr black holes exist only below this line in the grey region. The yellow region represents hairy Kerr black hole solutions, bounded by the red line (solitonic limit with $q = 1$ and $r_H = 0$), the green line (extremal hairy black holes with $q \neq 0$), and blue lines for cloud solutions ($q = 0$).

Dotted lines represent sequences of solutions with constant horizon radii, while red dots indicate specific black hole solutions used in the construction of accretion disks. A broader region of existence in ω_s is observed for black holes with smaller r_H values, which approaches the solitonic and extremal limits as the horizon radius tends to zero. For each fixed r_H, the track begins at the Minkowski limit ($\omega_s/\mu = 1$) and ends at the cloud line.

3 Calculating the image of the accretion disk

3.1 Circular Orbits on the Equatorial Plane

The study of stable circular orbits near black holes is crucial for revealing their observational characteristics. The innermost stable circular orbit (ISCO) represents the minimum radius at which a stable orbit can exist and is often interpreted as the boundary of the inner edge of the accretion disk. As charged particles move in orbit around the black hole, they emit synchrotron radiation, which is linked to the frequency of the geodesic at the ISCO [38]. This allows for the determination of the physical properties of the black hole through observations of the ISCO and the accretion disk.

To evaluate the ISCO, we start by considering the line element of Eq. (7) in the form

$$ds^2 = g_{tt}dt^2 + g_{rr}dr^2 + g_{\theta\theta}d\theta^2 + g_{\phi\phi}d\phi^2 + 2g_{t\phi}dtd\phi. \tag{9}$$

Due to the stationarity and axisymmetry of the spacetime, both $p_t = -E$ and $p_\phi = L$ are conserved quantities of the geodesic motion for a particle with four-velocity u^μ. Therefore, we have

$$u^t = \frac{g_{t\phi}L + g_{\phi\phi}E}{g_{t\phi}^2 - g_{tt}g_{\phi\phi}}, \quad u^\phi = -\frac{g_{tt}L + g_{t\phi}E}{g_{t\phi}^2 - g_{tt}g_{\phi\phi}}. \tag{10}$$

Taking into account that, for the particle's motion, the four-velocity norm is $u^\mu u_\mu = -\epsilon$, with $\epsilon = \{0, 1\}$ for a massless and massive particle, respectively, one can derive the radial equation of motion, which in the equatorial plane ($\theta = \pi/2$) reduces to

$$\dot{r}^2 = V_{eff} = \frac{1}{g_{rr}}\bigg(-\epsilon + \frac{E^2 g_{\phi\phi} + 2EL g_{t\phi} + L^2 g_{tt}}{g_{t\phi}^2 - g_{tt} g_{\phi\phi}} \bigg), \tag{11}$$

where we define the effective potential V_{eff}. The conditions for the existence of a circular orbit are $\dot{r} = 0$ and $\ddot{r} = 0$, which simultaneously reduce to $V_{eff} = 0$ and $\partial_r V_{eff} = 0$ at the constant orbital radius. These conditions further simplify to the following algebraic relations that must be satisfied for circular orbits:

$$E^2 g_{\phi\phi} + 2EL\, g_{t\phi} + L^2 g_{tt} - \epsilon\,(g_{t\phi}^2 - g_{tt} g_{\phi\phi}) = 0, \tag{12}$$

$$E^2 \partial_r g_{\phi\phi} + 2EL\, \partial_r g_{t\phi} + L^2 g_{tt} - \epsilon\, \partial_r (g_{t\phi}^2 - g_{tt} g_{\phi\phi}) = 0. \tag{13}$$

For a massive particle, the innermost stable circular orbit (ISCO) is located at a saddle point of the effective potential, requiring the additional condition $\partial_r^2 V_{eff} = 0$. Consequently, the equation

$$E^2 \partial_r^2 g_{\phi\phi} + 2EL\, \partial_r^2 g_{t\phi} + L^2 g_{tt} - \epsilon\, \partial_r^2 (g_{t\phi}^2 - g_{tt} g_{\phi\phi}) = 0, \tag{14}$$

together with the previously mentioned constraints, must be satisfied at $r = r_{isco}$. Thus, for each particle moving on a circular orbit with radius and orbital angular frequency $\Omega := u^\phi / u^t$, the energy and angular momentum are uniquely determined by these two constraints, as follows:

$$E = -\frac{g_{tt} + g_{t\phi}\Omega}{\sqrt{-g_{tt} - 2g_{t\phi}\Omega - g_{\phi\phi}\Omega^2}}, \tag{15}$$

$$L = \frac{g_{t\phi} + g_{\phi\phi}\Omega}{\sqrt{-g_{tt} - 2g_{t\phi}\Omega - g_{\phi\phi}\Omega^2}}, \tag{16}$$

The orbital angular frequency of particles at both the ISCO and the light circular orbits, known as light rings, is given by

$$\Omega = \frac{-\partial_r g_{t\phi} \pm \sqrt{\partial_r g_{t\phi}^2 - \partial_r g_{tt} \partial_r g_{\phi\phi}}}{\partial_r g_{\phi\phi}}, \tag{17}$$

where the plus sign corresponds to the angular frequency of co-rotating particles, while the minus sign corresponds to the angular frequency of counter-rotating particles.

3.2 Radiation from a Thin Accretion Disk

We investigate the emission characteristics of a thin accretion disk and its observable image as viewed from a distance, utilizing the Novikov-Thorne framework [39, 40]. This model represents the disk as an anisotropic fluid restricted to the equatorial plane, with a vertical thickness much smaller than its horizontal dimensions, maintained in a state of hydrodynamic equilibrium. The physical behavior of the disk is described by structural equations derived from the conservation principles of rest mass, energy, and angular momentum. These principles allow for the calculation of the energy flux radiated by the disk, spanning the region from the ISCO to a radial distance r, which corresponds to a circumferential radius of $\tilde{r} = 30M$, as given by

$$F(r) = -\frac{c^2 \dot{M}}{4\pi\sqrt{-g^{(3)}}} \frac{\partial_r \Omega}{(E - \Omega L)^2} \int_{r_{isco}}^{r} (E - \Omega L) \partial_r L \, dr. \tag{18}$$

The determinant of the induced metric in the equatorial plane is denoted as $g^{(3)}$, $\dot{M}$ is the mass accretion rate, and E, L, and Ω represent the energy, angular momentum, and angular velocity of particles on circular orbits. For steady-state models, the accretion rate is constant and depends on the central compact object. Kinematic quantities vary with orbital radius and are explicitly given by the Eqs. (15), (16) and (17).

Since, for Kerr black holes with scalar hair, the flux scales with the black hole's mass and accretion rate, we define a normalized flux, $\tilde{F}$, to facilitate the comparison of profiles obtained from spacetimes with different spin parameters, as follows [41]:

$$F(r) = \frac{c^2 \dot{M}}{M_g^2} \tilde{F}(r), \tag{19}$$

where $M_g = GM/c^2$ and M is the ADM mass of the black hole solution. In Fig. 2 the normalized fluxes $\tilde{F}(r)$ are shown for the chosen configurations $\mathbf{I}^0_{0.05}$, $\mathbf{II}^0_{0.1}$ and $\mathbf{III}^0_{0.2}$.

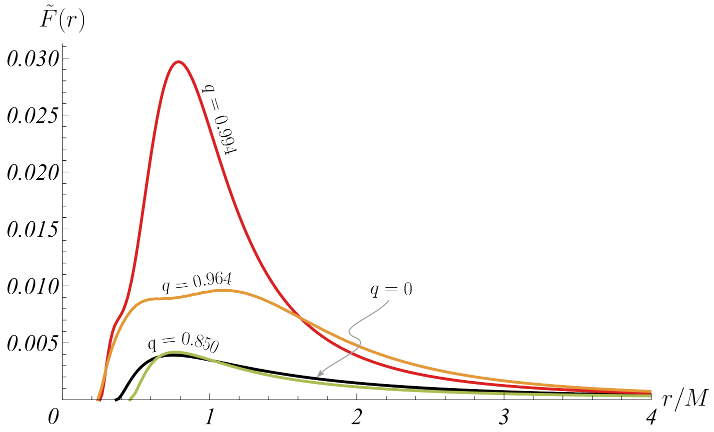

Figure 2: The normalized radial energy fluxes $\tilde{F}(r)$ for the configurations $\mathbf{I}^0_{0.05}$, $\mathbf{II}^0_{0.1}$ and $\mathbf{III}^0_{0.2}$ highlighted in Fig. 1 each characterized by normalized charges $q = 0.994489$, $q = 0.964476$ and $q = 0.850778$, respectively, as shown in Table 1 of the Appendix. For comparison, the radial energy flux of a Kerr black hole ($q = 0$) is represented by the black curve.

3.3 Ray Tracing

To determine the paths of light rays, the photon's initial conditions are required: $\{x^\mu(\lambda), p^\mu(\lambda)\}|_{\lambda=0}$, where λ represents the geodesic affine parameter. These initial conditions are derived using a local orthonormal basis at the observer's position, located at $\tilde{r}_{obs} = 200M$ and $\theta_{obs} = 80°$. The circumferential radius $\tilde{r}$ is computed from the coordinate radius r [35]. The initial 4-momentum of the photon is obtained following the method in [16], with the angles α and β parameterizing the impact parameters at the observer's location:

$$x = -\tilde{r}_{obs} \tan\beta, \qquad y = \tilde{r}_{obs} \sin\alpha. \tag{20}$$

The observer, positioned at $(\tilde{r}_{obs}, \theta_{obs})$, views a two-dimensional flat screen (x, y) oriented perpendicular to the line connecting the observer and the black hole center. Each pair of angles α and β uniquely determines a photon trajectory. The components of the photon's 4-momentum are given by:

$$E = \frac{1 + \gamma\sqrt{g_{\phi\phi}}\sin\beta\cos\alpha}{\zeta}, \qquad p_r = \sqrt{g_{rr}}\cos\beta\cos\alpha, \tag{21}$$

$$L = \sqrt{g_{\phi\phi}}\sin\beta\cos\alpha, \qquad p_\theta = \sqrt{g_{\theta\theta}}\sin\alpha, \tag{22}$$

with

$$\gamma = -\zeta\,\frac{g_{t\phi}}{g_{\phi\phi}}, \qquad \zeta = \sqrt{\frac{g_{\phi\phi}}{g_{t\phi}^2 - g_{tt}g_{\phi\phi}}}. \tag{23}$$

The conserved quantities $E = -p_t$ and $L = p_\phi$ have been employed wherever needed.

With the observer positioned at $\tilde{r}_{obs} = 200M$ and an inclination angle $\theta = 80°$, the angles α and β are used to calculate the impact parameters (x, y) and the photon's initial momenta within a local orthonormal frame. From this setup, photon trajectories are traced backward in time. These paths either terminate at the thin accretion disk, which lies in the equatorial plane ($\theta_{disk} = \pi/2$) and spans the region $\tilde{r}_{isco} < \tilde{r} < \tilde{r}_{out}$, or lead to the black hole horizon r_H. The accretion disk's outer edge is set at a circumferential radius of $\tilde{r}_{out} = 30M$.

3.4 Apparent Radiation Flux

The radiation flux will appear deformed to a distant observer, as its apparent intensity F_{obs} in each point of the observer's sky will be modified by a factor depending on the gravitational redshift z [42]:

$$F_{obs} = \frac{\tilde{F}}{(1+z)^4}. \tag{24}$$

To a distant observer, the radiation flux will appear distorted due to the gravitational redshift. The observed intensity, F_{obs}, at each point on the observer's sky will be affected by a factor that depends on the gravitational redshift z:

$$1 + z = \frac{1 + \Omega\,\xi}{\sqrt{-g_{tt} - 2g_{t\phi}\Omega - g_{\phi\phi}\Omega^2}}, \tag{25}$$

where $\xi = L/E$ is the impact parameter of the light ray and L and E are calculated using the expressions in Eqs. (21) and (22). For clearer illustration of the distribution, the normalized and cube-rooted apparent radiation flux for configurations $\mathbf{I}^0_{0.05}$, $\mathbf{II}^0_{0.1}$ and $\mathbf{III}^0_{0.2}$ is shown on Figs. 3, 4 and 5.

4 Conclusion

In summary, the results indicate that for extremely high values of the normalized charge ($q = 0.994$) in the presented model $\mathbf{I}$ ($r_H = 0.05$ and $q \simeq 0.994$), the accretion disk exhibits extensive regions of chaotically scattered geodesics. This behavior results in the formation of multiple disconnected indirect images of the accretion disk. In this case, the maximum apparent energy flux reaches its highest value

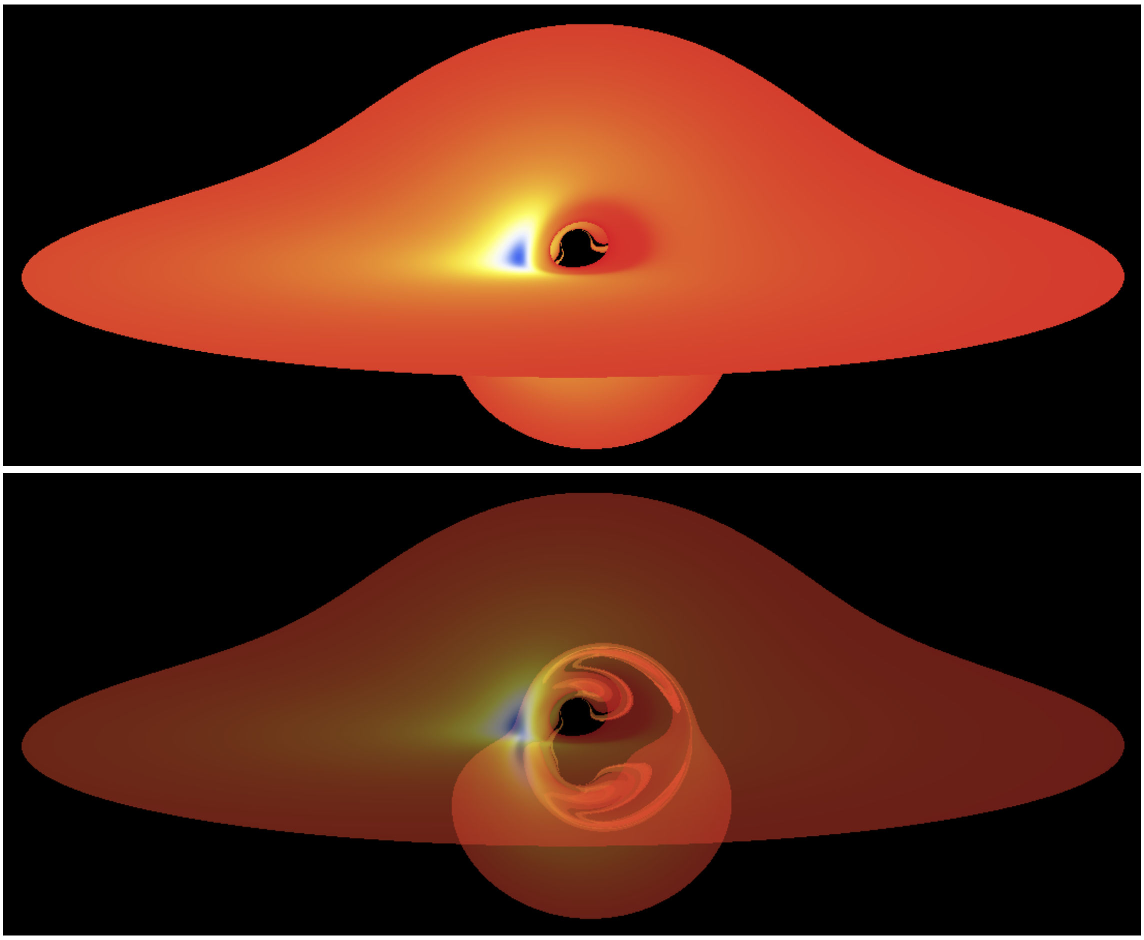

Figure 3: Examples of images of thin accretion disks at zero Gaussian curvature ($\kappa = 0$) of the target space with a black hole horizon radius of $r_H = 0.05$, viewed by an observer at an inclination angle of $\theta_{obs} = 80°$, are presented. These images correspond to the configuration $\mathbf{I}^0_{0.05}$ with $\omega_s/\mu = 0.706$, $M\mu = 0.908$, and $q = 0.994$. In the image above, the accretion disk is depicted as optically opaque, whereas in the image below, a 50% transparent representation reveals both the direct and indirect relativistic images of the disk. Detailed physical properties of these configurations are provided in Table 1 in Appendix A.

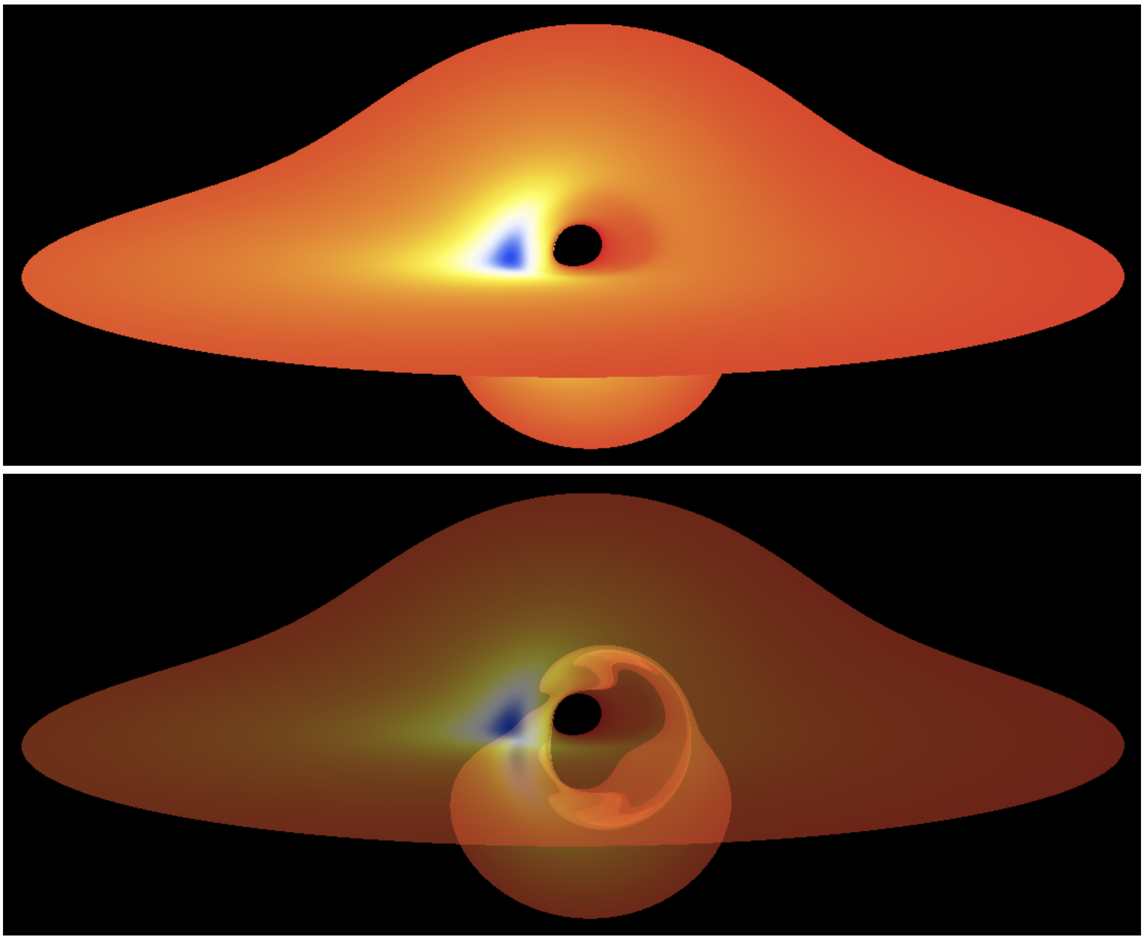

Figure 4: Examples of images of thin accretion disks at zero Gaussian curvature ($\kappa = 0$) of the target space with a black hole horizon radius of $r_H = 0.1$, viewed by an observer at an inclination angle of $\theta_{obs} = 80^\circ$, are presented. These images correspond to the configuration $\mathbf{II}^0_{0.1}$ with $\omega_s/\mu = 0.738$, $M\mu = 1.000$ and $q = 0.964$. In the image above, the accretion disk is depicted as optically opaque, whereas in the image below, a 50% transparent representation reveals both the direct and indirect relativistic images of the disk. Detailed physical properties of these configurations are provided in Table 1 in Appendix A.

among all the studied scenarios, amounting to $F_{max} = 7.98 \times 10^{-2} M\dot{M}$.

At moderately lower values of the normalized charge in model **II** ($r_H = 0.1$ and $q = 0.964$), the flux distribution becomes more compact, reaching a maximum value of $F_{max} = 2.51 \times 10^{-2} M\dot{M}$. The disk image features fewer disconnected components and a clearly defined dominant shadow component.

Finally, in model **III**, for a black hole with $r_H = 0.2$ and normalized charge value near $q = 0.851$, the configuration features a single ergoregion with deformed, quasi-circular shadows, where the chaotic scattering of geodesics becomes negligible. At even lower values of q, the accretion disk image of hairy black holes consists of a single oval shadow component. The apparent flux decreases further, reaching a relatively smaller value of $F_{max} = 9.82 \times 10^{-3} M\dot{M}$ compared to higher normalized charges. In this scenario, the image qualitatively resembles that of a Kerr black hole, where the maximum apparent flux reaches a significantly lower value of $F_{max} = 2.35 \times 10^{-4} M\dot{M}$.

A Physical quantities of selected solutions

We provide a detailed description of the solutions used to create the black hole thin accretion disks. These solutions are taken from [29], where sequences with fixed horizon radii were analyzed for zero Gaussian curvature κ.

Table 1: Physical quantities of hairy black hole solutions, as shown in Fig. 1, correspond to a zero Gaussian curvature of the target space, $\kappa = 0$. Each configuration is labeled as $\mathbf{X}^0_v$, where $\mathbf{X}$ denotes the configuration number, the superscript 0 specifies the Gaussian curvature κ, and the subscript v indicates the black hole horizon radius r_H.

Label	ω_s/μ	$M\mu$	$J\mu^2$	$M_{BH}\mu$	$J_{BH}\mu^2$	$M_\psi\mu$	$J_\psi\mu^2$	J_ψ/J	J/M^2	J_{BH}/M_{BH}^2
$\mathbf{I}^0_{0.05}$	0.706	0.908	0.833	0.025	0.004	0.942	0.828	0.994	0.892	7.131
$\mathbf{II}^0_{0.1}$	0.739	1.000	0.854	0.087	0.030	0.913	0.823	0.964	0.853	3.998
$\mathbf{III}^0_{0.2}$	0.896	0.879	0.679	0.280	0.101	0.599	0.578	0.851	0.879	1.295

Acknowledgements

This study is financed by the European Union-NextGenerationEU, through the National Recovery and Resilience Plan of the Republic of Bulgaria, project No. BG-RRP-2.004-0008-C01. DD acknowledges

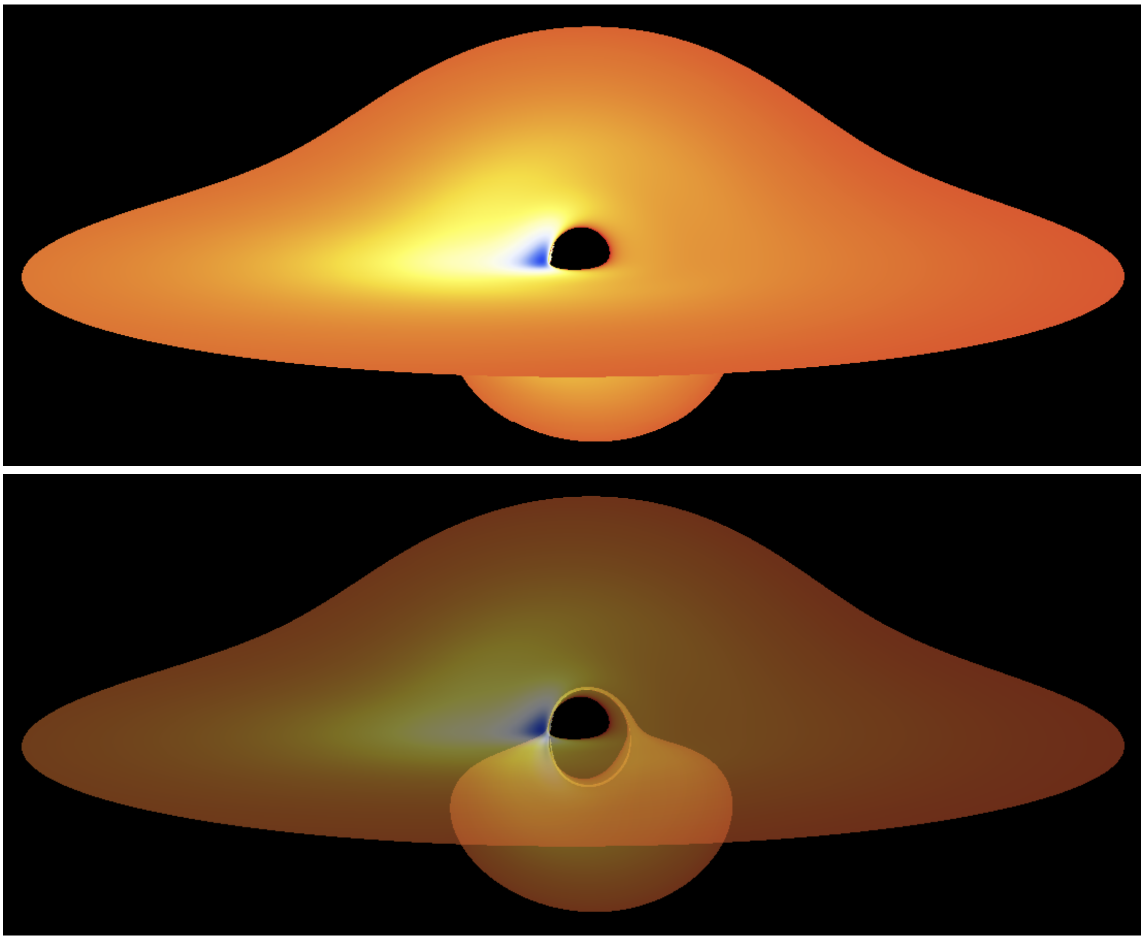

Figure 5: Examples of images of thin accretion disks at zero Gaussian curvature ($\kappa = 0$) of the target space with a black hole horizon radius of $r_H = 0.2$, viewed by an observer at an inclination angle of $\theta_{obs} = 80^\circ$, are presented. These images correspond to the configuration $\mathbf{III}^0_{0.2}$ with $\omega_s/\mu = 0.896$, $M\mu = 0.879$ and $q = 0.851$. In the image above, the accretion disk is depicted as optically opaque, whereas in the image below, a 50% transparent representation reveals both the direct and indirect relativistic images of the disk. Detailed physical properties of these configurations are provided in Table 1 in Appendix A.

financial support via an Emmy Noether Research Group funded by the German Research Foundation (DFG) under grant no. DO 1771/1-1.

References

[1] Event Horizon Telescope Collaboration et al. First M87 event horizon telescope results. iv. imaging the central supermassive black hole. *arXiv:1906.11241*, 2019.

[2] Event Horizon Telescope Collaboration et al. First sagittarius A* event horizon telescope results. ii. eht and multiwavelength observations, data processing, and calibration. *The Astrophysical Journal Letters*, 930(2):L13, may 2022.

[3] Rajibul Shaikh. Shadows of rotating wormholes. *Phys. Rev. D*, 98:024044, 2018.

[4] Nobuyuki Sakai, Hiromi Saida, and Takashi Tamaki. Gravastar Shadows. *Phys. Rev. D*, 90(10):104013, 2014.

[5] Galin Gyulchev, Petya Nedkova, Vassil Tinchev, and Stoytcho Yazadjiev. On the shadow of rotating traversable wormholes. *Eur. Phys. J. C*, 78(7):544, 2018.

[6] Hyat Huang, Jutta Kunz, Jinbo Yang, and Cong Zhang. Light ring behind wormhole throat: Geodesics, images, and shadows. *Phys. Rev. D*, 107(10):104060, 2023.

[7] Hyat Huang, Jutta Kunz, and Deeshani Mitra. Shadow images of compact objects in beyond Horndeski theory. 2024.

[8] Leonardo Amarilla, Ernesto F. Eiroa, and Gaston Giribet. Null geodesics and shadow of a rotating black hole in extended chern-simons modified gravity. *Phys. Rev. D*, 81:124045, 2010.

[9] Leonardo Amarilla and Ernesto F. Eiroa. Shadow of a rotating braneworld black hole. *Phys. Rev. D*, 85:064019, 2012.

[10] Leonardo Amarilla and Ernesto F. Eiroa. Shadow of a kaluza-klein rotating dilaton black hole. *Phys. Rev. D*, 87:044057, 2013.

[11] Pedro V.P. Cunha, Carlos A.R. Herdeiro, Burkhard Kleihaus, Jutta Kunz, and Eugen Radu. Shadows of Einstein–dilaton–gauss–bonnet black holes. *Physics Letters B*, 768:373–379, 2017.

[12] Mingzhi Wang, Songbai Chen, and Jiliang Jing. Chaotic shadow of a non-Kerr rotating compact object with quadrupole mass moment. *Phys. Rev. D*, 98(10):104040, 2018.

[13] Yehui Hou, Minyong Guo, and Bin Chen. Revisiting the shadow of braneworld black holes. *Phys. Rev. D*, 104(2):024001, 2021.

[14] Zhenyu Zhang, Yehui Hou, and Minyong Guo. Observational signatures of rotating black holes in the semiclassical gravity with trace anomaly, 2023.

[15] Pedro VP Cunha, Carlos AR Herdeiro, Eugen Radu, and Helgi F Rúnarsson. Shadows of kerr black holes with scalar hair. *Physical review letters*, 115(21):211102, (2015).

[16] Pedro VP Cunha, Carlos AR Herdeiro, Eugen Radu, and Helgi F Runarsson. Shadows of kerr black holes with and without scalar hair. *International Journal of Modern Physics D*, 25(09):1641021, (2016).

[17] P. V. P. Cunha, J. Grover, C. Herdeiro, E. Radu, H. Rúnarsson, and A. Wittig. Chaotic lensing around boson stars and kerr black holes with scalar hair. *Phys. Rev. D*, 94:104023, (2016).

[18] Carlos AR Herdeiro and Eugen Radu. Kerr black holes with scalar hair. *Physical review letters*, 112(22):221101, 2014.

[19] Carlos Herdeiro and Eugen Radu. Construction and physical properties of kerr black holes with scalar hair. *Classical and Quantum Gravity*, 32(14):144001, 2015.

[20] Thibault Damour and Gilles Esposito-Farese. Tensor multiscalar theories of gravitation. *Class. Quant. Grav.*, 9:2093–2176, 1992.

[21] Michael Horbatsch, Hector O Silva, Davide Gerosa, Paolo Pani, Emanuele Berti, Leonardo Gualtieri, and Ulrich Sperhake. Tensor-multi-scalar theories: relativistic stars and 3+1 decomposition. *Classical and Quantum Gravity*, 32(20):204001, 2015.

[22] Ivo Sengo, Pedro V. P. Cunha, Carlos A. R. Herdeiro, and Eugen Radu. Kerr black holes with synchronised Proca hair: lensing, shadows and EHT constraints. *JCAP*, 01:047, 2023.

[23] Daisuke Nitta, Takeshi Chiba, and Naoshi Sugiyama. Shadows of colliding black holes. *Phys. Rev. D*, 84:063008, 2011.

[24] Akifumi Yumoto, Daisuke Nitta, Takeshi Chiba, and Naoshi Sugiyama. Shadows of multi-black holes: Analytic exploration. *Phys. Rev. D*, 86:103001, 2012.

[25] Jake O Shipley and Sam R Dolan. Binary black hole shadows, chaotic scattering and the cantor set. *Classical and Quantum Gravity*, 33(17):175001, 2016.

[26] Shohreh Abdolrahimi, Robert B. Mann, and Christos Tzounis. Distorted local shadows. *Phys. Rev. D*, 91:084052, 2015.

[27] Shohreh Abdolrahimi, Robert B. Mann, and Christos Tzounis. Double images from a single black hole. *Phys. Rev. D*, 92:124011, 2015.

[28] Jai Grover, Jutta Kunz, Petya Nedkova, Alexander Wittig, and Stoytcho Yazadjiev. Multiple shadows from distorted static black holes. *Phys. Rev. D*, 97(8):084024, 2018.

[29] Lucas G Collodel, Daniela D Doneva, and Stoytcho S Yazadjiev. Rotating tensor-multiscalar black holes with two scalars. *Physical Review D*, 102(8):084032, 2020.

[30] Shahar Hod. Stationary scalar clouds around rotating black holes. *Physical Review D*, 86(10):104026, 2012.

[31] Shahar Hod. Stationary resonances of rapidly-rotating kerr black holes. *The European Physical Journal C*, 73:1–5, 2013.

[32] Carolina L Benone, Luís CB Crispino, Carlos Herdeiro, and Eugen Radu. Kerr-newman scalar clouds. *Physical Review D*, 90(10):104024, 2014.

[33] Shahar Hod. The large-mass limit of cloudy black holes. *Classical and Quantum Gravity*, 32(13):134002, 2015.

[34] Carlos AR Herdeiro and Eugen Radu. Asymptotically flat black holes with scalar hair: a review. *International Journal of Modern Physics D*, 24(09):1542014, 2015.

[35] Galin Gyulchev, Ayush Roy, Lucas Collodel, Petya Nedkova, Stoytcho Yazadjiev and Daniela Doneva, Shadows of rotating hairy Kerr black holes coupled to time periodic scalar fields with a nonflat target space, *Phys. Rev. D*, 109:104051, 2024, doi: 10.1103/PhysRevD.109.104051.

[36] Stoytcho S. Yazadjiev and Daniela D. Doneva. Dark compact objects in massive tensor-multi-scalar theories of gravity. *Physical Review D*, 99(8):084011, 2019.

[37] Lucas G. Collodel, Daniela D. Doneva, and Stoytcho S. Yazadjiev. Rotating tensor-multiscalar solitons. *Physical Review D*, 101(4):044021, 2020.

[38] Pedro G. S. Fernandes, David J. Mulryne. A new approach and code for spinning black holes in modified gravity, Class. Quantum Grav. 40, 165001 (2023).

[39] Novikov, I., Thorne, K. Les Houches Summer School of Theoretical Physics: Black Holes (New York: Gordon and Breach), 343 (1973).

[40] Page, D. N., Thorne, K. S. Disk-Accretion onto a Black Hole. Time-Averaged Structure of Accretion Disk, ApJ, 191, 499 (1974).

[41] Lucas G. Collodel, Daniela D. Doneva and Stoytcho S. Yazadjiev. Circular Orbit Structure and Thin Accretion Disks around Kerr Black Holes with Scalar Hair, ApJ, Volume 910, Issue 1, id.52, 11 pp. (2021).

[42] Luminet, J. P. Image of a spherical black hole with thin accretion disk, Astron. Astrophys. **75**, 228 (1979).